High-Order Accurate CFD/CSD Simulation of the UH-60 Rotor in Forward Flight

Jasim U. Ahmad[1] and Neal M. Chaderjian[2]
NASA Ames Research Center, Moffett Field, CA 94035

Time-dependent Reynolds-averaged Navier-Stokes simulations for a highly flexible aeroelastic UH-60A rotor have been carried out for forward flight. The fluid structure interaction is accomplished by loosely coupling the OVERFLOW Computational Fluid Dynamics (CFD) code with the helicopter comprehensive code CAMRAD II. The latter includes Computational Structural Dynamics (CSD) with rotor trim capability. Computations are performed using spatial differences of 5th-order for inviscid fluxes, 2nd-order accurate viscous fluxes, and 2nd-order time accuracy. Dual time-stepping accuracy is examined and recommendations provided for an appropriate time step and number of subiterations. The predicted sectional normal forces and pitching moments are compared with flight-test data for high-speed and low-speed level-flight conditions. The low-speed case has significant Blade Vortex Interaction (BVI). The current simulations demonstrate a factor of two improvement in state-of-the-art airloads prediction accuracy for CFD/CSD simulations. This is attributed to the use of improved spatial accuracy.

I. Introduction

COMPUTATIONAL Fluid Dynamics (CFD) simulation of rotorcraft flow fields using the Reynolds-averaged Navier-Stokes (RANS) equations is a challenging multidisciplinary problem. This is primarily due to the need to model the aeroelastic interaction of the fluid dynamics with highly flexible rotor blades. A successful aerodynamic simulation of a rotor/fuselage system requires the modeling of unsteady three-dimensional flows that may include transonic shocks, dynamic stall with boundary layer separation, complex vortical wakes, blade/wake and wake/wake interactions, and body motions. Moreover, a stable and robust method to couple the CFD with a Computational Structural Dynamics (CSD) model is required. Consequently, the aerodynamic and aeroacoustic performance prediction for rotorcraft lags compared to its fixed-wing counterpart.

The helicopter industry often uses comprehensive rotor codes as part of the design process. These comprehensive codes typically include a simplified linear aerodynamic model, a CSD method for flexible rotor blades, and a trim algorithm. However, this very efficient design tool lacks the high fidelity aerodynamics needed for nonlinear rotorcraft flows. It is common at NASA and in the rotorcraft industry to carry out a parameter sweep of rotorcraft simulations with a less computationally costly comprehensive code, such as CAMRAD II,[1] when linear aerodynamics is sufficiently accurate. When nonlinear aerodynamics is important, coupled simulations are carried out using a more computationally costly CFD code, such as OVERFLOW,[2-3] together with a comprehensive code. The idea is to replace the linear aerodynamics in the comprehensive code with the nonlinear aerodynamics provided by the high-fidelity CFD code through the loose-coupling process.

One of the goals of NASA's Subsonic Rotary Wing (SRW) Project, which is part of NASA's Fundamental Aeronautics Program, is to develop physics-based computational tools to address the challenges and accuracy requirements of aeromechanics simulation. Yamauchi and Young[4] recently reported on the state-of-the-art (SOA) of aeromechanics simulation. This assessment found that the current SOA CFD prediction of rotor normal force differs from experiment by about $M^2C_n \approx 4.4\%$, and the computed pitching moment differs from experiment by about $M^2C_m \approx 4.7\%$. These values were obtained by comparing computed and experimental sectional values from different CFD simulations and experiments as a function of azimuth for one rotor revolution. Details of this comparison process are described in Ref. 4.

An example of a SOA simulation coupling CFD and CSD for a flexible UH-60A rotor is reported by Potsdam et

[1] Aerospace Engineer, Applied Modeling and Simulation Branch, M/S 258-2.

[2] Research Scientist, Fundamental Modeling and Simulation Branch, M/S 258-2, Associate Fellow AIAA.

al.[5] They used the OVERFLOW-D overset CFD code to examine three different cases with different grid resolutions and mixed temporal/spatial accuracy. They solved the RANS equations on body-conforming curvilinear grids using 1st-order temporal accuracy and 2nd-order spatial accuracy. The inviscid Euler equations were solved on the off-body Cartesian grids using 3rd-order temporal and spatial accuracy. The 3rd-order spatial accuracy consisted of a 4th-order accurate central difference with a 3rd-order accurate artificial dissipation term. These Cartesian off-body grids are used to resolve the rotor wake and extend the computational domain to the far field. The inviscid higher-order accuracy in the rotor wake region was used to minimize vortex diffusion. One way to improve upon these rotor simulations is to use higher-order spatial accuracy. It is anticipated that this will improve the computed vortex strength generated at the rotor tip, and better preserve the vortex strength within the complex rotor wake region. This can be especially important when there is significant Blade Vortex Interaction (BVI). The overall result should be an improved prediction of time-dependent rotor loads.

OVERFLOW[2-3] is a state-of-the-art CFD code developed at NASA that solves the time-dependent RANS equations in generalized curvilinear coordinates using overset grids. A recent upgrade (Version 2.2) includes up to 6th-order spatial accuracy using central differences.[6] This updated CFD code has been loosely coupled with the CAMRAD II helicopter comprehensive code to take advantage of CAMRAD's CSD and trim capability. The work reported here simulates a flexible rotor flowfield using high-order spatial differencing. Details of the spatial accuracy are described in the Flow-Solver Algorithm section. The goal is to demonstrate an improvement over the SOA loads prediction accuracy by at least 20% for the UH-60A Airloads database.[7] The database provides aerodynamic pressures, structural loads, control positions, and rotor forces and moments. Two level flight conditions are chosen from this database, i.e., flight counter C8513 and C8534. Flight counter C8534 is a high-speed level-flight condition, while flight counter C8513 is a low-speed case with significant BVI. The BVI case is considered more difficult to accurately simulate than the high-speed case.

The numerical approach is described in the next section, followed by a discussion of results and concluding remarks.

II. Numerical Approach

The numerical approach described below includes a brief description of the CAMRAD II comprehensive code, the fluid/structure loose coupling procedure, the UH-60A geometry and overset grids, and the OVERFLOW CFD code.

A. Comprehensive Code: CSD and Rotor Trim

The comprehensive code CAMRAD II[1] developed at NASA performs structural dynamics and rotor trim for a coupled CFD/CSD simulation. This code is widely used in the helicopter industry. It models the flexible blade structure using nonlinear finite elements. CAMRAD II has its own simplified aerodynamic lifting-line model with airfoil table lookup, as well as simplified wake models. Although this code has been widely used, its prediction capability is limited due to the low fidelity aerodynamic modeling. However, it has been used with high-fidelity CFD models in a loosely coupled manner. The details of this comprehensive code are described in Ref. 1, and the coupling strategy is described below and in Ref. 5.

B. Fluid/Structure Interaction: Loose Coupling

For static flight conditions, a loose coupling between CFD and CSD is employed, as the interaction between the structure and aerodynamic response is not necessary at every flow solver time step. This coupling is done in a periodic manner, as specified by the user. It is typical to couple the CFD and CSD once every revolution, or some fraction of a revolution based on the number of rotor blades. For example, a four-blade rotor may be coupled every ¼, ½, or full revolution. Quicker fluids/structures convergence may be obtained by more frequent coupling. However, depending on the flow conditions, too frequent a coupling may result in a divergent process. At each coupling step, CFD rotor loads are provided to CAMRAD and, in turn, it uses these CFD loads to make a correction to its own lifting-line aerodynamics model to re-trim the rotor. CAMRAD then provides a new rotor-blade deflection file to the CFD code. When this loosely coupled process is fully converged, the CFD airloads have fully replaced the comprehensive analysis airloads.

Figure 1 shows a flow chart for the loose coupling iterative procedure. The detailed logistics for running the coupled CAMRAD and OVERFLOW process is accomplished using a C-shell script. This script helps automate the run process, which uses many CAMRAD tools. The reader is again referred to Refs. 1, 5 for additional details.

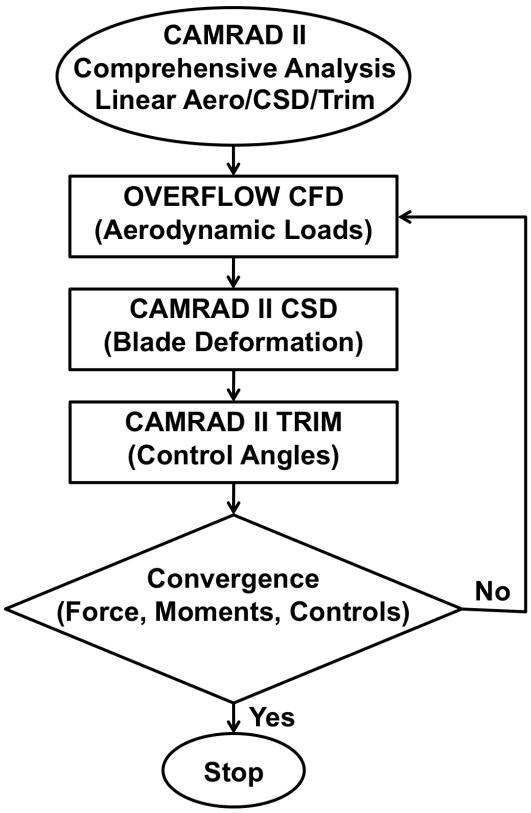

Figure 1. Loose coupling procedure with OVERFLOW and CAMRAD II.

C. Rotor Geometry/CFD Grid

The overset grid system used in the present simulations was generated using Chimera Grid Tools (CGT).[8] The CGT contains a very efficient and modular grid scripting library used for grid manipulation, generation, reorganization, overset hole cutting surfaces, and generation of OVERFLOW input files. This scripting procedure allows one to produce high quality surface grids and subsequent volume grids with a set of input parameters. These input parameters allow one to quickly and automatically modify the grid system for the existing geometry.

The UH-60A rotor blade is highly twisted. A schematic of the geometry and the O-grid system used in the present simulations is shown in Fig. 2. The blade surface definition is provided in PLOT3D format.[3] The blade tip geometry is faithfully represented in the surface grid, including all sharp edges. The blade root is extended inboard towards the hub. The overset grids for each rotor blade consist of three separate grids: the main rotor-blade body, a cap grid at the outboard tip, and a cap grid at the inboard root. All three grids use an O-mesh topology that maintains good surface resolution. Each blade surface mesh consists of approximately 114 thousand points. In the present simulations, an idealized hub is placed at the center of the rotor-blade system. This provides a more realistic flow condition along the rotor spin axis, without the complication of generating grids about the actual UH-60A hub geometry. "Near-body" grids refer to the curvilinear overset grids attached to the rotor/hub bodies. These are imbedded into Cartesian "off-body" grids that resolve the rotor wake region and extend the computational domain to the far field. These off-body Cartesian grids are automatically generated within OVERFLOW according to user specified input parameters. Moreover, the off-body Cartesian grids are generated at various levels of resolution starting from "Level 1" (L_1) in the rotor-wake region, to successively coarser grid levels to rapidly and efficiently extend the grid system to the far field. For this study, the L_1 vortex-wake grid spacing is set to $0.1c_{tip}$, where c_{tip} is the rotor tip chord length. The far-field boundaries are about five rotor radii from the rotor center. The overset mesh for the rotor, idealized hub and automatically generated off-body grids consists of approximately 69 million grid points. The body grids are about 50% of the total grid size. The viscous spacing provides an average $y^+ \approx 0.1$ near the outboard tip. The rotor-blade schematic, Fig. 2c, shows spanwise stations where loads will be compared with flight-test data.

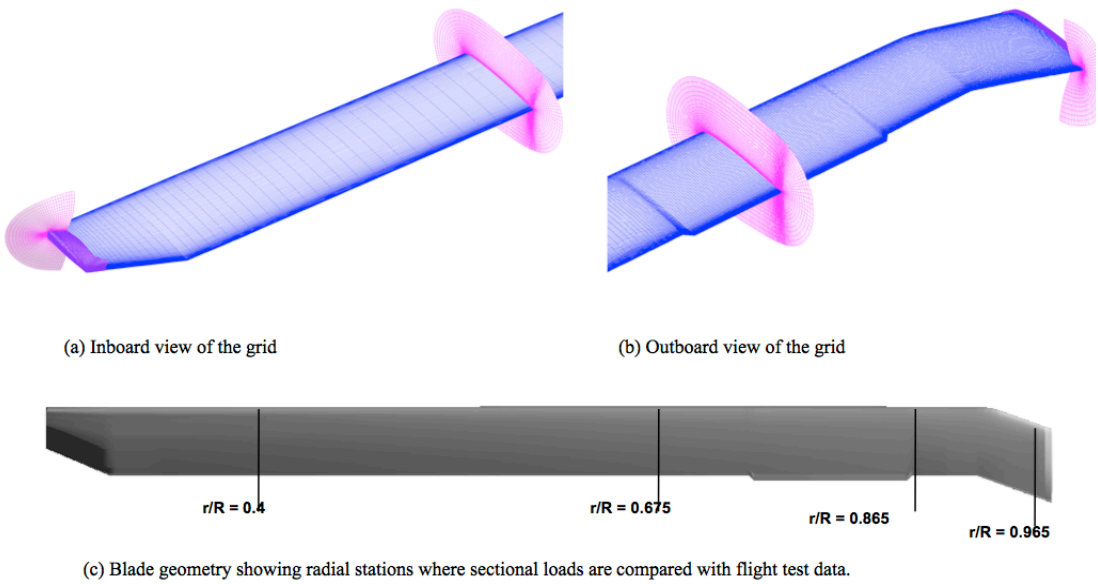

(a) Inboard view of the grid

(b) Outboard view of the grid

(c) Blade geometry showing radial stations where sectional loads are compared with flight test data.

Figure 2. Blade grid and surface geometry.

D. Flow-Solver Algorithm

OVERFLOW is a finite-difference, overset grid, RANS CFD code. Up to 6th-order spatial accuracy for inviscid fluxes and 2nd-order time accuracy are available.[6] OVERFLOW has two modes of operation, stationary grids and dynamic grid motions. In the case of grid movement, both rigid-body motions and deforming grids are permitted. Inter-grid overset communication can be established external to OVERFLOW using the PEGASUS code.[9] This is only done for non-moving grid cases. For the present dynamically moving grid simulations, inter-grid communication is established using X-Rays[3] and the very efficient Domain Connectivity Function[3] within OVERFLOW. OVERFLOW has several turbulence models available. For the present study, the one-equation Spalart-Allmaras model[10] is used. OVERFLOW has many flow-solver options described in Refs. 2-3. The effect of subiteration convergence on temporal accuracy is quantified in the Results section.

A 2nd-order accurate dual time-stepping algorithm is used to solve the RANS equations, and is based on the dual time-stepping methods described in Refs. 11-12. The dual time-stepping algorithm is now described, and subiteration accuracy is discussed in the results section.

The RANS equations can be written in strong conservation-law form as

$$\frac{\partial Q}{\partial t}+\frac{\partial (F-F_v)}{\partial x}+\frac{\partial (G-G_v)}{\partial y}+\frac{\partial (H-H_v)}{\partial z}=0 \tag{1}$$

where $Q=\left[\rho \quad \rho u \quad \rho v \quad \rho w \quad e\right]^{\mathrm{T}}$ is the vector of conserved variables; F, G, and H are the inviscid flux vectors; and F_v, G_v, and H_v are the viscous flux vectors.

An artificial time term is introduced to the governing equations in order to provide a relaxation (subiteration) procedure between physical time steps.

$$\frac{\partial Q}{\partial \tau}+\frac{\partial Q}{\partial t}+\frac{\partial (F-F_v)}{\partial x}+\frac{\partial (G-G_v)}{\partial y}+\frac{\partial (H-H_v)}{\partial z}=0 \tag{2}$$

where t corresponds to physical time and τ corresponds to artificial (pseudo) time.

First-order accurate Euler implicit differencing is used for the artificial time discretization, while a second-order accurate three-point backward difference is used for the physical time discretization. An implicit approximate factorization form of Eq. (2) in generalized coordinates is given by

$$\left[I+h\partial_{\xi}\hat{A}^{k}\right]\left[I+h\partial_{\eta}\hat{B}^{k}\right]\left[I+h\partial_{\zeta}\hat{C}^{k}\right]\Delta\hat{Q}^{k}=-hR^{k,n} \tag{3}$$

where

$$R^{k,n} = \frac{3\hat{Q}^k - 4\hat{Q}^n + \hat{Q}^{n-1}}{2\Delta t} + \left(\hat{F} - \hat{F}_v\right)_\xi^k + \left(\hat{G} - \hat{G}_v\right)_\eta^k + \left(\hat{H} - \hat{H}_v\right)_\zeta^k$$

and

$$h = \frac{2\Delta t \Delta\tau}{2\Delta t + 3\Delta\tau}$$

In these equations, $\hat{Q} = Q/J$, where J is the transformation Jacobian, and A, B, and C are the inviscid flux Jacobians. The variable k is the subiteration index, while the variable n is the time-step index. Finally, $\Delta\hat{Q}^k = \hat{Q}^{k+1} - \hat{Q}^k$. Subiteration convergence implies that $\hat{Q}^k \to \hat{Q}^{n+1}$, which is second order accurate in time.

A diagonalized implicit algorithm[13] is used to solve this equation, and central differences are used to discretize the spatial derivatives. Upwind difference options are available in OVERFLOW, but were not used in this study.

The dual time-stepping algorithm has three main advantages over a single time-stepping approach. It is more robust, allows for larger time steps, and the subiteration procedure eliminates the factorization and linearization errors in the diagonalized approximate factorization algorithm. However, one must be careful to verify that enough subiteration steps are taken to ensure adequate subiteration convergence to the new time step. If the residual drop at each subiteration is not sufficient, then the resulting simulation is not time accurate.

The spatial accuracy consists of evaluating the convective terms with 6th-order central differences and 5th-order artificial dissipation. This results in a 5th-order discretization on the uniform Cartesian off-body grids. However, all viscous terms are evaluated with 2nd-order accurate central differences. The grid metrics on the curvilinear near-body grids are also 2nd-order accurate in space. This discretization is referred to as 5th-order spatial differencing throughout this paper. Although the algorithm is still formally 2nd-order accurate in space, this differencing scheme has lower diffusion and dispersion errors, and an improved flow field resolution than a 3rd-order approach. Further details are described by Pulliam.[6]

III. Results

NASA and the US Army, as a part of the UH-60A Airloads program, maintain a unique and extensive flight-test database[7] for level flight and transient maneuvers. The database provides aerodynamic pressures, structural loads, control positions, and rotor forces and moments. This database is extensively used for the validation of both aerodynamic and structural models. The test matrix provides a range of flight conditions.[1,7] This study presents results for two flight counters. Flight counter C8534 is a high-speed level-flight case that is used for analysis and verification for Fluid Structure Interaction [FSI] phase lag problems. Flight counter C8513 is a low-speed case with significant BVI.

The high-speed flight counter C8534 is considered the easier of the two cases presented in this paper. The advance ratio is $\mu = 0.37$, the freestream Mach number is M_∞=0.236, and the tip Mach number is M_{tip}=0.64. Reference 7 mentions that many investigations have been performed on this flight-test counter to understand unsolved analysis problems for the advancing blade azimuthal phase lag and underprediction of blade pitching moments. A fuselage was not included in these simulations.

Figure 3 shows a top view of the vortex wake for flight counter C8534. Notice how quickly the vortex cores are swept downwind. Note also how the 5th-order spatial differences provide good resolution of the rotor blades' wake shear layers as they convect downwind.

The vortex cores shown in Fig. 3 are rendered using iso-surfaces of the Q-criterion density (Q_d). This is given by the expression

$$Q_d = \frac{\left\|\Omega_{ij}\right\|^2 - \left\|S_{ij}\right\|^2}{\left\|\Omega_{ij}\right\|^2 + \left\|S_{ij}\right\|^2} = -\frac{\left(\frac{\partial u_i}{\partial x_j}\right)\left(\frac{\partial u_j}{\partial x_i}\right)}{\left(\frac{\partial u_i}{\partial x_j}\right)\left(\frac{\partial u_i}{\partial x_j}\right)} \tag{4}$$

where $\left\|S_{ij}\right\|$ and $\left\|\Omega_{ij}\right\|$ are the magnitudes of the strain-rate and spin tensors, respectively. The Q-criterion density provides a convenient way to visualize vortices. This nondimensional quantity has a range of $-1 \le Q_d \le 1$. Since Q_d is computed from tensors, it is also invariant with coordinate rotations.

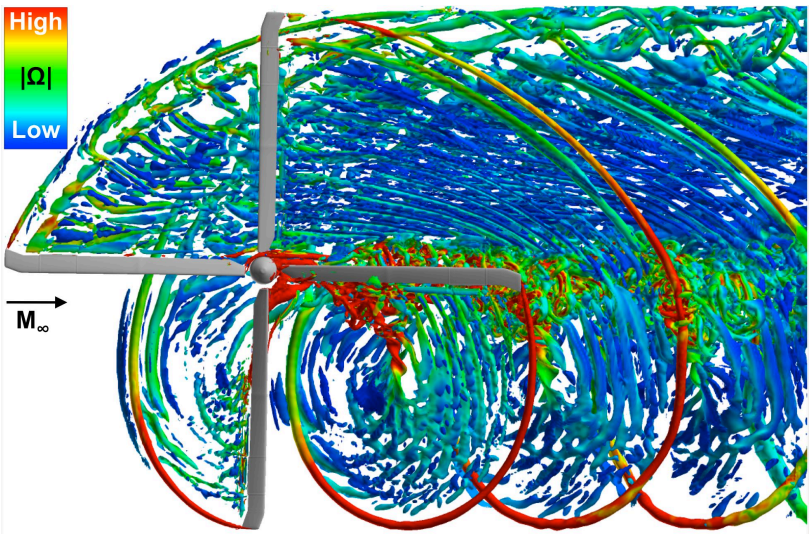

Figure 3. Top view of vortices visualized with the Q-criterion density. High-speed case, flight counter C8534, M_∞=0.236, μ = 0.37.

The effect of time step and number of dual-time subiterations required for time accuracy was examined for the high-speed case. This was accomplished by varying the physical time step from the reference value (Δt_0=¼° blade rotation) and the number of subiterations from the reference value (k_0=35), see Eq. 3. These reference values were originally chosen from experience to provide time accurate results. The structural deflections are converged for the reference conditions, and used throughout this time-accuracy study. The fundamental waveform variation of the lift, drag, pitching and yawing moments with the number of subiterations and time step was examined. The total rotor pitching moment coefficient (C_M) variation with azimuth angle is shown in Fig. 4a. The azimuth angle, ψ, is proportional to time and shown in Fig. 4b. There are four similar waveforms per blade revolution (one for each blade). The last waveform is shown in Fig. 4a. The most notable differences in the waveforms occur near ψ=330°, where the most converged result, k=70, differs markedly from the first few results, k=5, 10, 15, …

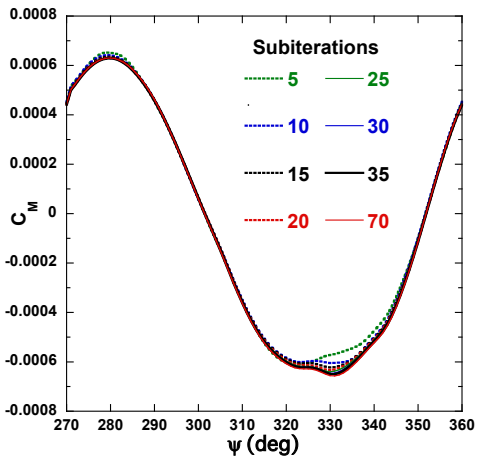

(a) C_M waveform variation with dual-time subiteration.

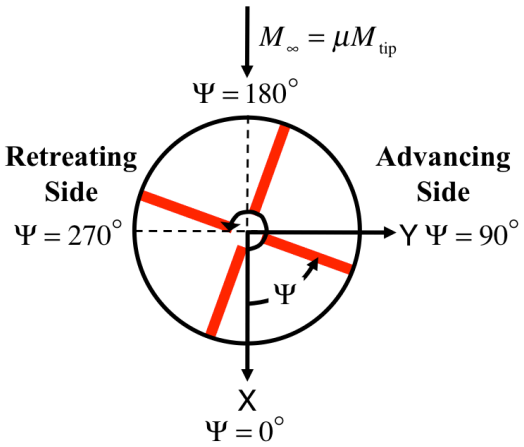

(b) Sketch of rotor axis system.

Figure 4. High-speed case flight counter C8534, M_∞=0.236, μ = 0.37.

The root-mean-square (RMS) error between the computed waveform and the most converged waveform ($\Delta t=\Delta t_0/4$, k=70) for the lift, drag, pitching and yawing moments is shown in Fig. 5. This provides a quantitative measure of how dual-time subiterations affect time accuracy. Notice that of the four force and moment coefficients examined, the pitching moment coefficient has the largest RMS error. The pitching moment coefficient will therefore be the focus of this time-accuracy study. The goal is to obtain an RMS error of less than 1% in C_M with the least amount of computational work. A study has been performed for the other forces and moments with similar results.

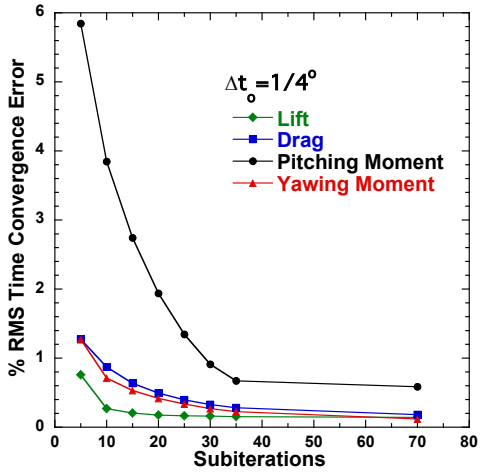

Figure 5. Force and moment variation with dual-time subiteration. High-speed case flight counter C8534, M_∞=0.236, μ = 0.37.

Figure 6 shows how the %RMS error in C_M varies with physical time step and the number of dual-time subiterations. Notice that the three smallest time steps in Fig. 6 were able to achieve an RMS error of less than 1%, but the largest time step, $\Delta t=2\Delta t_0$, was unable to do so. In fact, the largest time step indicates a tendency to diverge with a large number of subiterations.

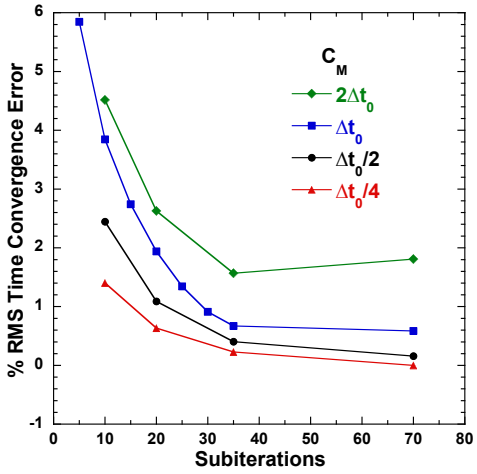

Figure 6. Percent RMS error of C_M with time step and dual-time subiteration. High-speed case flight counter C8534, M_∞=0.236, μ = 0.37.

The relative Optimal Computational Work (OCW) needed to achieve less than 1% RMS error in C_M is used to quantify the computational efficiency of the dual-time procedure. In this case, "optimal" means achieving a 1% RMS target error while advancing the flow solution with the smallest amount of CPU wallclock time. The computational work is proportional to the total number of steps and processors, i.e., (number of time steps/revolution) × (number of dual-time subiterations) × (No. CPUs). The relative OCW is defined as the ratio of the optimal computational wallclock time and a reference value, and is given by the expression

$$\text{Relative OCW} = \frac{\left(\dfrac{k_{optimal}\cdot \text{No. CPU}}{\Delta t}\right)}{\left(\dfrac{k_o\cdot \text{No. CPU}_o}{\Delta t_o}\right)} = \frac{\left(\dfrac{k_{optimal}}{k_o}\right)}{\left(\dfrac{\Delta t}{\Delta t_o}\right)}\left(\frac{\text{No. CPU}}{\text{No. CPU}_o}\right) \tag{5}$$

where k_{optimal} is the least number of subiterations needed to achieve a 1% RMS error. In this study, the number of CPUs is kept fixed, so (No. CPU/No. CPU_o)=1.

Table 1 shows that the least amount of computational work needed to obtain a CFD solution is obtained by using the reference time step and subiterations, i.e., k=35, Δt=¼°. For this case, using a smaller time step requires fewer dual-time subiterations to achieve a 1% RMS error in C_M. However, the amount of computational work is still larger than the reference value because there are more time steps per rotor revolution. The optimal choice of the original reference parameters is attributed to user experience. The reference values, k_o=35 and Δt_o=¼°, are used for both flight counter cases presented in this paper. The number of L_1 Cartesian grid cells traversed by the rotor tip for each time step is also listed in Table 1. Notice that the largest time step, which had a tendency for subiteration divergence (see Fig. 6), caused the rotor tip to traverse more than one Cartesian grid cell during a time-step advance. For the other time steps, the rotor tip traveled less than one grid cell during a time-step advance. The tendency to diverge is attributed to excessive L_1 grid-cell travel.

$\Delta t/\Delta t_o$	Subiterations ($k_{optimal}$)	Relative OCW (Less Than 1% RMS Error)	Rotor Tip Travel (L_1 Grid Cells)
0.25	20	2.29	0.17
0.50	27	1.54	0.34
1.00	35	1.00	0.68
2.00	NA	Error never less than 1%	1.35

Table 1. Relative OCW needed to obtain less than 1% RMS error in C_M, and blade-tip travel. High-speed case C8534, M_∞=0.236, μ = 0.37, k_0=35, Δt_0=¼°.

This time-accuracy study suggests that larger time steps tend to result in less computational work while maintaining time accuracy. However, if the time step is too large, dual-time convergence may suffer or even diverge. A rule of thumb is to use the largest time step possible that resolves all frequencies of interest, and that has less than one L_1 Cartesian grid-cell travel by the rotor tip, and use the smallest number of subiterations for a desired level of temporal convergence (time accuracy).

Now that time accuracy has been established, the computational sectional loads for the high-speed case (C8534) are compared to the UH-60A airloads data.[7] The blade motions (and resultant loads) are trimmed to the measured thrust and upper shaft bending moments. The non-dimensional sectional forces and moments, M^2C_n and M^2C_m, are normalized by the speed of sound rather than the local sectional velocity in order to compare sectional values in a global sense.

Following conventional rotorcraft nomenclature, ψ = 0 corresponds to the blade span pointing in the direction of the freestream velocity. For the advancing side of the blade motion, e.g., ψ = 90 degrees, the rotor blade leading edge experiences a relative flow consisting of the freestream plus the rotational speed, while for the retreating side, e.g., ψ = 270 degrees, the relative flow consists of the freestream minus the rotational speed. Airload comparisons between computation and experiment have the mean removed due to uncertainty in the measured data.[5,7]

Figures 7 and 8, respectively, show the sectional pitching moment and sectional normal force coefficient variation with azimuth angle, ψ, at different radial stations, see Fig. 2c. The pitching moments at the inboard sections, r/R = 0.40 and 0.675, are in good agreement with the flight-test data. There are no significant wake-blade interactions. The pitching moments at the section immediately following the trim tab, r/R=0.865, as well as the outboard section, r/R=0.965, show some differences due to negative loading on the advancing side. Overall, the agreement is fairly good. The normal forces show very similar trends and are in overall good agreement with the flight-test data.

Figure 9 shows the loose coupling convergence for both normal force and pitching moments at a radial station of r/R = 0.965. Each of the cycles represents one loose coupling per ½ revolution. Convergence takes longer on the advancing side of the rotor disk, i.e., 90°≤ψ≤180°. The CFD and CSD interaction is fully converged after 6 or 7 cycles.

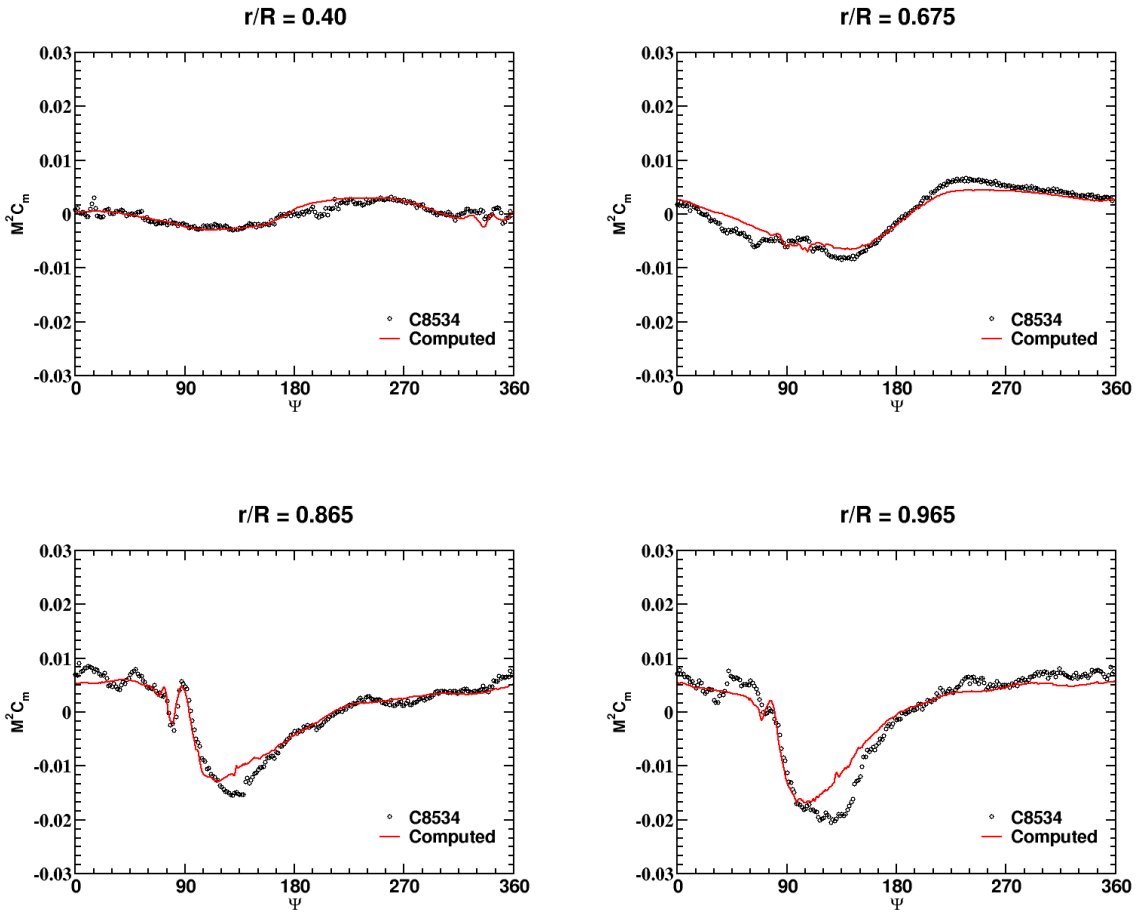

Figure 7. Pitching moment coefficient variation with azimuth angle at various radial stations. High-speed case, flight counter C8534, M_∞=0.236, μ = 0.37.

The goal of improving the SOA prediction accuracy in normal force by 20% requires an overall error of less than 3.5%. The current simulation has been compared with experiment in the manner described in Ref. 4, and an overall error of 2.1% was achieved, well within the stated goal. A 20% improvement in the SOA prediction of pitching moment required 3.8% prediction accuracy. The current simulation is compared with experiment with an overall error of 2.5% in normal forces, also achieving the accuracy goal. This improvement in the SOA prediction accuracy is attributed to the use of 5th-order spatial differencing, rather than 3rd-order differencing which had typically been used in the past.

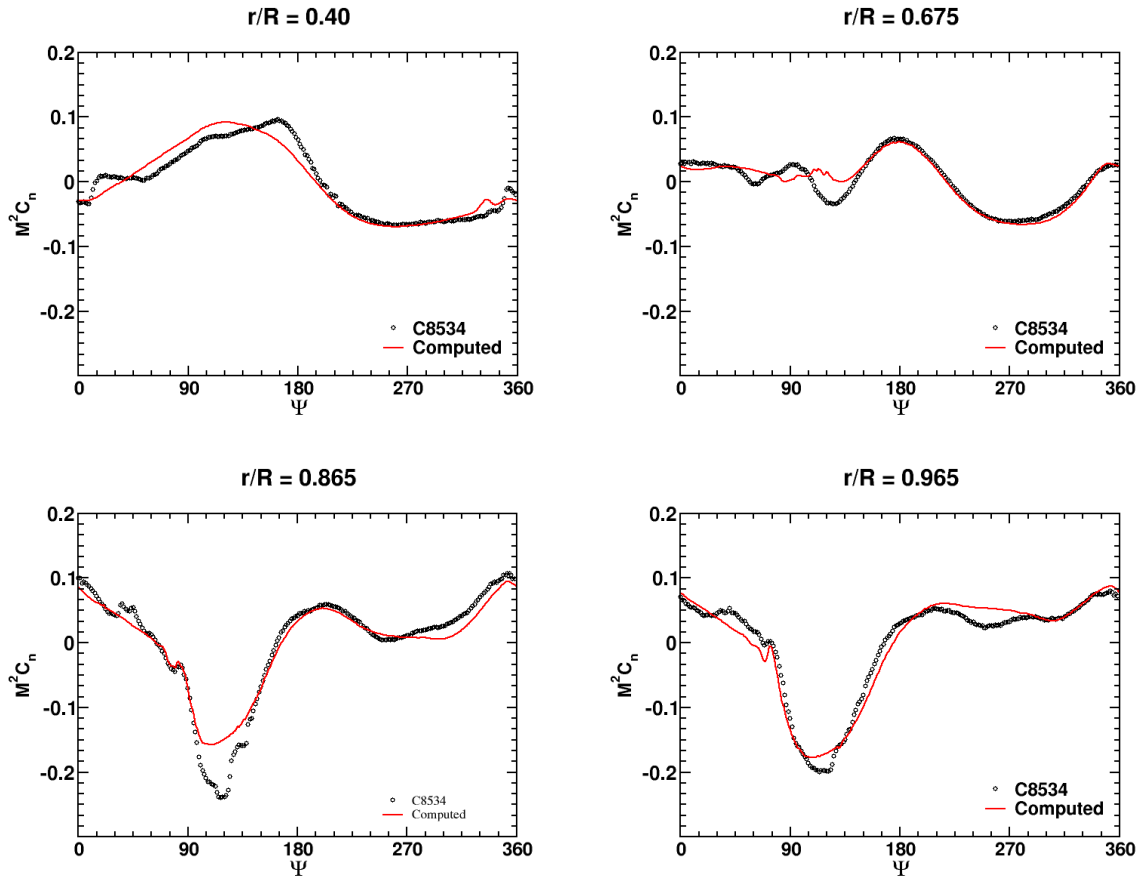

Figure 8. Normal force coefficient variation with azimuth angle at various radial stations. High-speed case, flight counter C8534, M_∞=0.236, μ = 0.37.

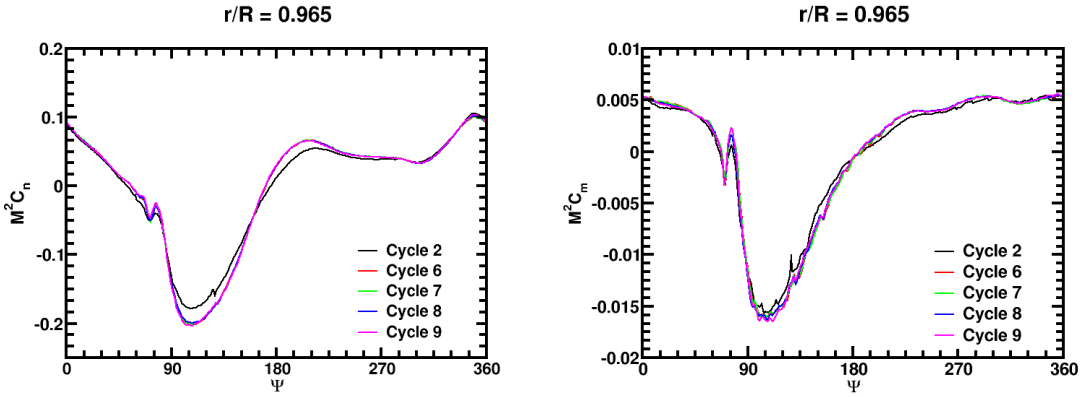

(a) Normal force convergence. (b) Pitching moment convergence.

Figure 9. CFD/CSD loose-coupling convergence. High-speed case, flight counter C8534, M_∞=0.236, μ = 0.37.

A second case is now presented. The flight counter C8513 corresponds to a level-flight condition with advance ratio of μ = 0.15. The freestream Mach number is M_∞=0.096. The airloads are dominated by the presence of BVI. The flow visualization presented in Figure 10 shows a very strong BVI in the top and oblique views. This BVI is observed in Fig. 10 by the rotor blades slicing through the vortex cores. The vortex cores are again rendered using iso-surfaces of the Q-criterion density. A transparent cutting plane, showing velocity magnitude contours, clearly shows the circumferential velocity fields generated by the vortices.

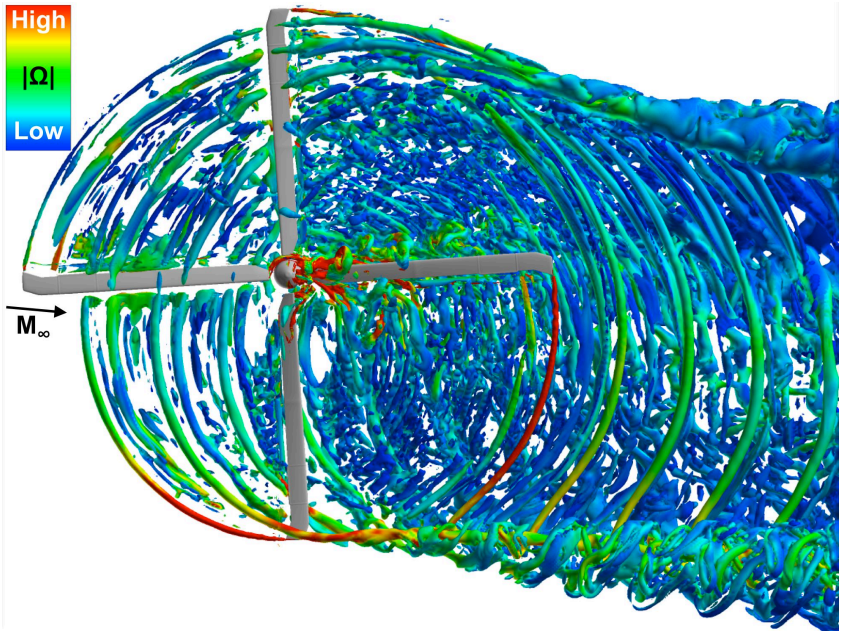

(a) Top view.

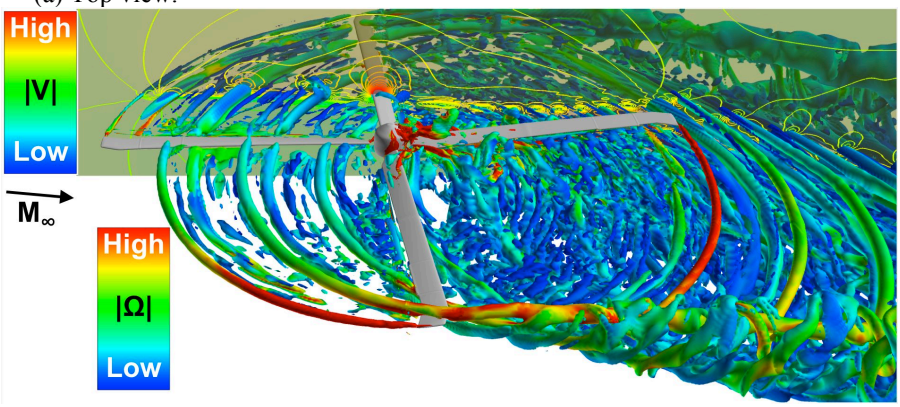

(b) Oblique view. Velocity magnitude shown on transparent cutting plane.

Figure 10. Vortices visualized with the Q-criterion density. BVI case, flight counter C8513, M_∞=0.096, μ = 0.15.

Figure 11 compares the computed sectional pitching moment coefficient with flight-test data at different radial stations, see Fig. 2c. At the inboard station, r/R = 0.40, the pitching moment compares very well with experiment. From the radial station, r/R = 0.675 and onward, the BVI events produce significant variations in pitching moment. Overall, the pitching moment compares well with flight-test data for this complex flow. At r/R = 0.675, prediction is better on the advancing side, ψ=90°, and somewhat underpredicted when the blade is retreating ψ=270°. At r/R = 0.865, the overall trends, including shape and magnitude, are reasonably captured at the advancing side, but the lower peak is underpredicted at the retreating side. At the outboard blade section, r/R = 0.965, there is a rapid variation in the pitching moment coefficient with azimuth angle, with strong sharp peaks. This is evidence of a very strong BVI. The computations compare well with the measured data and follow the general trends.

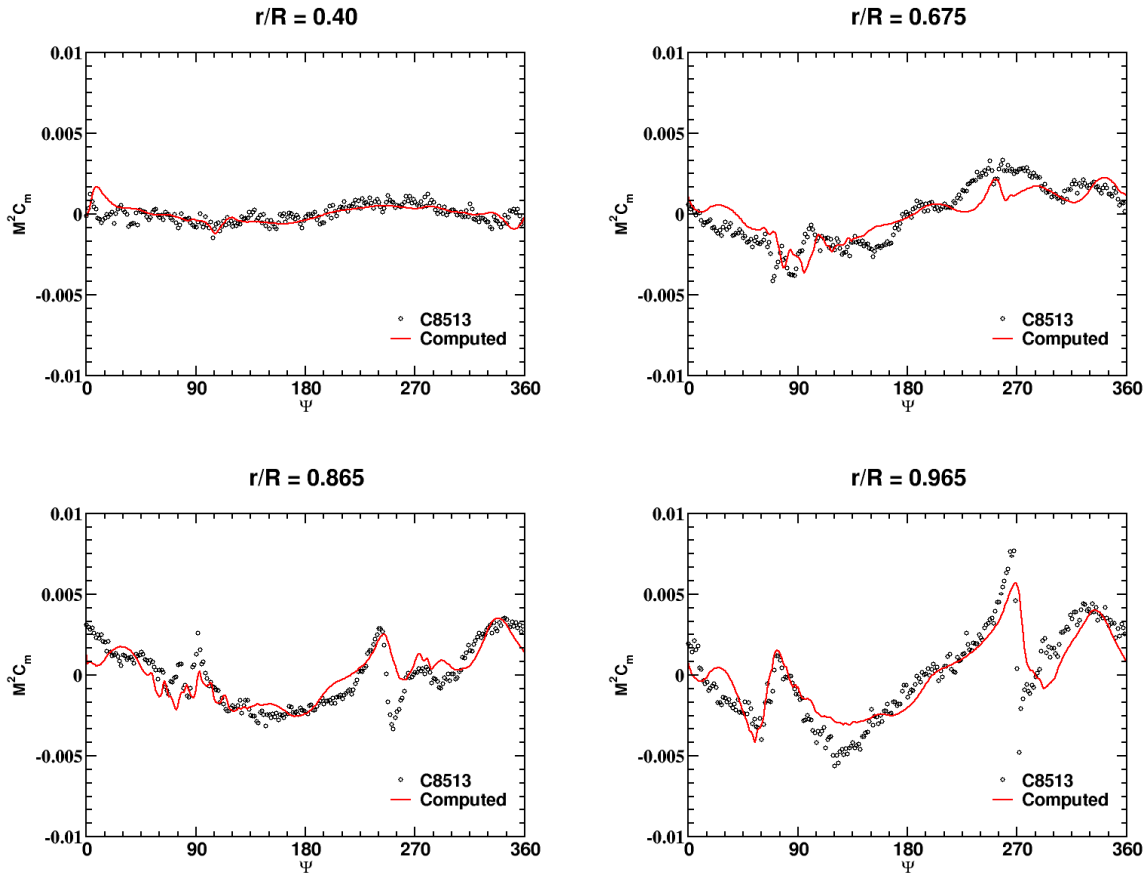

Figure 11. Pitching moment coefficient variation with azimuth angle at various radial stations. BVI case, flight counter C8513, M_∞=0.096, μ = 0.15.

Figure 12 compares the computed sectional normal force coefficient with flight-test data at different radial stations. The inboard variation of the normal force with azimuth angle compares very well with the flight-test data at r/R = 0.40 and 0.675. There is also a good comparison between the computed and measured normal force at the outboard stations, r/R = 0.865 and 0.965. The sharp peaks again indicate a strong BVI. There appears to be some phase error in the computed results at r/R = 0.865, near ψ=90°. There are several possible reasons for this discrepancy. There may be a need for more reference sections to transfer the CFD load to the CSD model, or higher-order time accuracy may be needed to reduce the convective error. The turbulence model may not be predicting the turbulent scales properly, or the measured data may also have some problems. Nevertheless, the computed normal force compares well with the flight-test data for this very complex CFD/CSD simulation.

Figure 13 shows the loose coupling convergence for both normal force and pitching moments at a radial station of r/R = 0.965. Each of the cycles represents one loose coupling per ½ revolution. Convergence takes longer on the advancing side of the rotor disk, i.e., 90°≤ψ≤180°. The CFD and CSD interaction is converged in less than 10 loose coupling cycles.

The goal of improving the SOA prediction accuracy in normal force and pitching moment by at least 20% was once again met as in the previous flight counter. The overall difference between computed and measured normal force and pitching moment, integrated over one rotor revolution, was 2.4% and 2.2%, respectively. This represents an improvement of about a factor of two over the SOA values of 4.4% and 4.7%.[4]

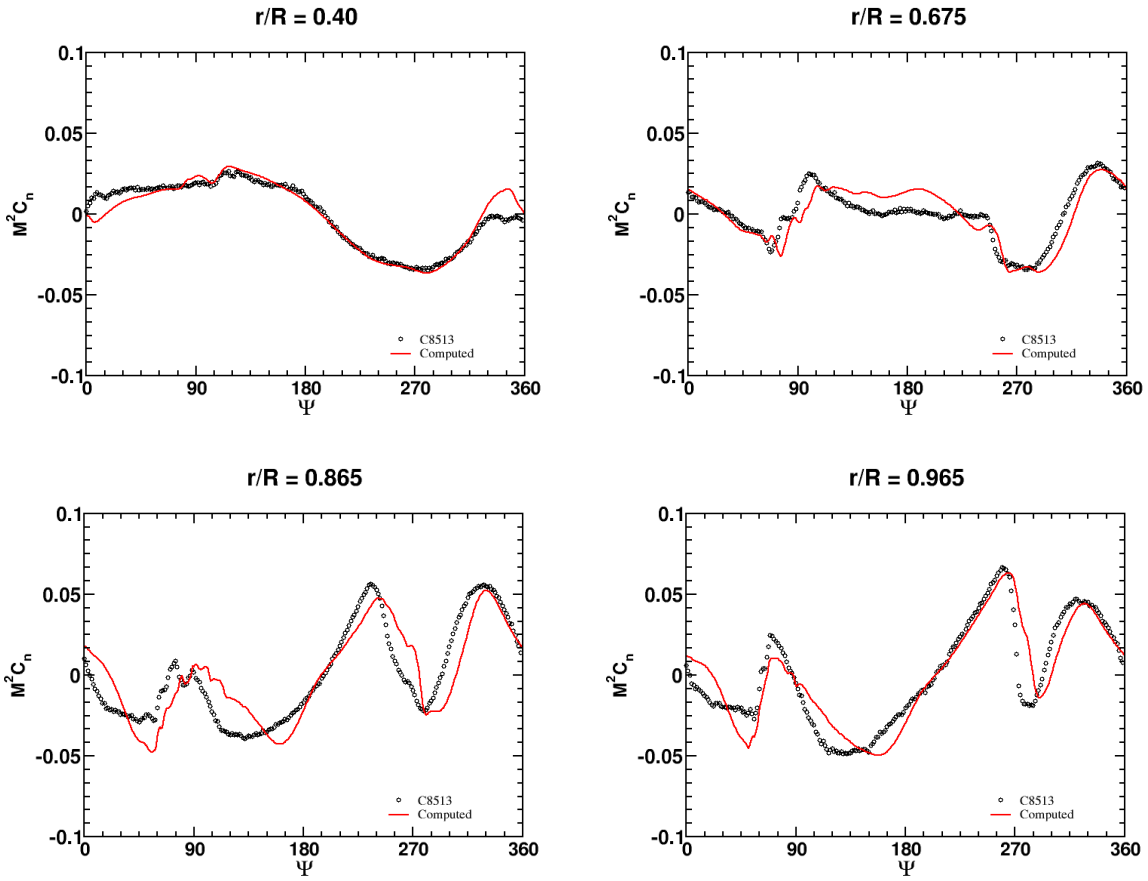

Figure 12. Normal force coefficient variation with azimuth angle at various radial stations. BVI case, flight counter C8513, M_∞=0.096, μ = 0.15.

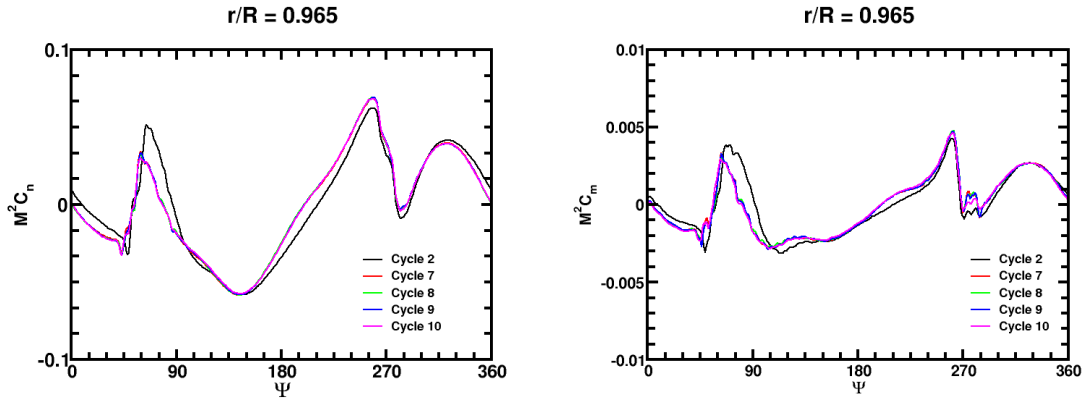

(a) Normal force convergence. (b) Pitching moment convergence.

Figure 13. CFD/CSD loose-coupling convergence. BVI case, flight counter C8513, M_∞=0.096, μ = 0.15.

IV. Summary and Conclusions

Time-dependent Reynolds-averaged Navier-Stokes simulations for a flexible UH-60A rotor have been carried out under high-speed and blade vortex interaction conditions. These aeroelastic simulations were obtained by loosely coupling the OVERFLOW CFD code with the CAMRAD II comprehensive CSD code. A study of dual-

time stepping accuracy was carried out and the following observations and recommendations are provided for efficient dual-time accuracy. Larger time steps with enough dual-time subiterations for convergence tend to result in less computational work while maintaining time accuracy. However, if the time step is too large, the dual-time process may diverge with an increased number of subiterations. It is also important to choose a time step that resolves all frequencies of interest while maintaining less than one L_1 Cartesian grid cell of travel by the rotor tip. Two flight counter cases, high-speed and BVI, were simulated and compared with available experimental data. The computed normal force and pitching moment coefficients were found to be in good agreement with flight-test data, and achieved a factor of two improvement in the state-of-the-art prediction accuracy. This improvement is attributed to using 5th-order spatial differences rather than 3rd-order spatial differences often used by other investigators.

References

[1]Johnson, W., "Rotorcraft Aerodynamic Models for a Comprehensive Analysis," American Helicopter Society 54th Annual Forum, Washington, D.C., May 1998.

[2]Nichols, R., Tramel, R., and Buning, P., "Solver and Turbulence Model Upgrades to OVERFLOW 2 for Unsteady and High-Speed Flow Applications," AIAA-2006-2824, June 2006.

[3]Nichols, R., and Buning, P., "User's Manual for OVERFLOW 2.1," University of Alabama at Birmingham, Birmingham, AL 35294.

[4]Gloria K. Yamauchi and Larry A. Young, "A Status of NASA Rotorcraft Research," NASA/TP–2009-215369, September, 2009.

[5]Potsdam, M., Yeo, H., and Johnson, W., "Rotor Airloads Prediction Using Loose Aerodynamic/Structural Coupling," *Journal of Aircraft*, Vol. 43, No. 3, May-June, 2006, pp. 732-742

[6]Pulliam, T. H., "High Order Accurate Finite-Difference Methods: as seen in OVERFLOW," to be presented at the 20th AIAA Computational Fluid Dynamics Conference, June 27-30, 2011, Honolulu, HI.

[7]Bousman, W. G. and Kufeld, R. M., "UH-60A Airloads Catalog," NASA TM 2005-212827, Aug. 2005.

[8]Chan, W.M., "Developments in Strategies and Software Tools for Overset Structured Grid Generation and Connectivity", to be presented at the AIAA 20th Computational Fluid Dynamics Conference, Honolulu, Hawaii, June 27-30, 2011.

[9]Rogers, S. E., Suhs, N. E., and Dietz, W. E., "PEGASUS 5: An Automated Pre-Processor for Overset-Grid CFD," *AIAA Journal*, Vol. 41, No. 6, June 2003, pp. 1037-1045.

[10]Spalart, P. R., and Allmaras, S. R., "A One-Equation Turbulence Model for Aerodynamic Flows," AIAA Paper 92-0439, January 1992.

[11]Pulliam, T. H., "Time Accuracy and the Use of Implicit Methods," AIAA Paper 93-3360, 1993.

[12]Venkateswaran, S., and Merkle, C. L., "Dual Time Stepping and Preconditioning for Unsteady Computations," AIAA Paper 95-0078, 1995.

[13]Pulliam, T. H., and Chaussee, D. S., "A Diagonal Form of an Implicit Approximate-Factorization Algorithm," *Journal of Computational Physics*, Vol. 39, No. 2, 1981, pp. 347-363.